Construction and Validation of an Urban Area Flow and Dispersion Model on Building Scales

CHEN Bicheng (陈笔澄), LIU Shuhua* (刘树华), MIAO Yucong (缪育聪), WANG Shu (王 姝), and LI Yuan (李 源)

Department of Atmospheric and Oceanic Sciences, School of Physics, Peking University, Beijing 100871

(Received January 25, 2013; in final form May 6, 2013)

ABSTRACT

This paper presents a numerical model that simulates the wind fields, turbulence fields, and dispersion of gaseous substances in urban areas on building to city block scales. A Computational Fluid Dynamics (CFD) approach using the steady-state, Reynolds-Averaged Navier-Stokes (RANS) equations with the standard k-ε turbulence model within control volumes of non-uniform cuboid shapes has been employed. Dispersion field is computed by solving an unsteady transport equation of passive scalar. Another approach based on Gaussian plume model is used to correct the turbulent Schmidt number of tracer, in order to improve the dispersion simulation. The experimental data from a wind tunnel under neutral conditions are used to validate the numerical results of velocity, turbulence, and dispersion fields. The numerical results show a reasonable agreement with the wind tunnel data. The deviation of concentration between the simulation with corrected turbulent Schmidt number and the wind tunnel experiments may arise from 1) imperfect point sources, 2) heterogeneous turbulent diffusivity, and 3) the constant turbulent Schmidt assumption used in the model.

Key words: urban areas, flow and dispersion, computational fluid dynamics, RANS equation, k-ε model, turbulent Schmidt number

Citation: Chen Bicheng, Liu Shuhua, Miao Yucong, et al., 2013: Construction and validation of an urban area flow and dispersion model on building scales. *Acta Meteor. Sinica*, **27**(6), 923–941, doi: 10.1007/s13351-013-0504-1.

1. Introduction

Dispersion of atmospheric pollutants in urban areas has been the subject of extended research in recent years, due to the increasingly imminent threat that the toxic gaseous substances may be intentionally or inadvertently released in a heavily populated urban environment.

There is a considerable amount of work dealing with flow and dispersion around buildings. Traditionally, the broad characteristics of flow and dispersion have been investigated mainly in the wind tunnel (e.g., Davidson et al., 1996; Gromke et al., 2008), where experimental conditions can be controlled. Some field trials (e.g., Higson et al., 1995; Macdonald et al., 1997; Mavroidis, 2000) have also been conducted in the real conditions of the atmosphere and on real scales, complementing the findings from wind tunnel experiments. Most wind tunnel and field experiments focused on isolated obstacles, arrays of obstacles, and two-dimensional street canyons, for the recognition that the interaction between buildings and flows could be possibly concluded with idealized models. Some studies (e.g., Macdonald et al., 1998; Mavroidis et al., 2003) compared results of wind tunnel and field experiments, and summarized that results from these two types of experiments mainly differ in the effect of wind meander and the larger scales of turbulence present in field trials. These studies have improved the understanding of the physical processes involved and provided necessary information for developing mathematical models as practical tools. However, both of them are considered to be costly, especially field trials, which require considerable time and effort since they

---

Supported by the China Meteorological Administration Special Public Welfare Research Fund (GYHY201106033).

*Corresponding author: lshuhua@pku.edu.cn.

are carried out in uncontrolled weather conditions. This weakness makes field trials difficult for practical purposes.

Recent advances in numerical modeling and computer capability lead to an increasing number of investigations on numerical simulation of urban area dispersion in a variety of controlled configurations, with some excellent reviews (e.g., Li et al., 2006) of atmospheric dispersion modeling. The flow, turbulence, and dispersion fields on the urban city block (1 km) to building scales (10 m) are directly influenced by the fine scale geometric features of the city. As a result, the models that accurately predict large scale dispersion based on simplified mathematic models, such as box models, Gaussian plume models, and Lagrangian puff models, are unable to predict accurately in urban areas. More sophisticated approaches, such as Computational Fluid Dynamics (CFD), capable of modeling the flow and the response of buildings to winds, are developed to simulate the urban area dispersion problems. There are a bunch of investigations about Reynolds-Averaged Navier-Stokes (RANS) based CFD (Krüs et al., 2003; Riddle et al., 2004; Coirier et al., 2005; Di Sabatino et al., 2007; Mavroidis et al., 2007; Santos et al., 2009; Tewari et al., 2010; Solazzo et al., 2011) as well as Large Eddy Simulation (LES) based CFD (Nozawa and Tamura, 2002; Cheng et al., 2003; Gousseau et al., 2011). Some studies even involved real complex urban-type geometries (Krüs et al., 2003; Hanna et al., 2006; Tewari et al., 2010). Clearly, the LES approach is better in prediction (Cheng et al., 2003; Gousseau et al., 2011), because it addresses many deficiencies brought about by the RANS models (namely, scale resolution). However, the LES simulations are computationally expensive, noted as "about 640 times greater than the k-ε model applied with wall functions and 26 times greater than the two-layer k-ε model" in Cheng et al. (2003). In view of this, the steady RANS based models appear to be a good compromise between solution accuracy and amount of computation.

This work aims to validate a newly built numerical model, based on the computational fluid dynamics approach. The model will be used to simulate the rapid responses of an urban environment to the lethal gas releasing events. Flow and turbulence fields are computed via steady RANS equations with standard k-ε turbulence model, and dispersion field is generated by an Eulerian-based transport equation. Details about the mathematic model and numerical methods are described in Sections 2 and 3, respectively. The results of the numerical simulation are validated by experimental data from wind tunnel experiments conducted by the Environmental Wind Tunnel Laboratory in University Hamburg in Section 4. An approach based on Gaussian plume model to improve the dispersion simulation is also provided in Section 4. Conclusions are given in Section 5.

2. Model description

Our approach is to generate the velocity and turbulence fields by solving the steady-state form RANS equations coupled with a standard k-ε model with suitable boundary conditions, and then compute the tracer concentration field by solving the unsteady Reynolds-averaged transport equation using the pre-computed velocity and turbulence fields.

2.1 Fundamental equations

The RANS equations are conservation equations derived by using the Reynolds decomposition with time averaging. Under the assumption of a high Reynolds number, the viscous term can be neglected, and the fluid flow can be considered to be unaffected by the concentration distribution since the magnitude of concentration is not sufficiently high to significantly alter the air density. Thus, the RANS equations are as follows in Cartesian tensor notation.

$$\frac{\partial(\rho\bar{u}_i)}{\partial x_i}=0, \tag{1}$$

$$\frac{\partial(\rho\bar{u}_i\bar{u}_j)}{\partial x_j}=-\frac{\partial\bar{p}}{\partial x_i}+\frac{\partial}{\partial x_j}(-\overline{\rho u_i' u_j'})-\rho g\delta_{i3}. \tag{2}$$

The equations shown here are for neutral conditions, where the buoyancy forces have been neglected. The variable $\bar{u}_i$ is the component of velocity in i-direction ($i=1$, 2, and 3 for directions x, y, and z, respectively), $\overline{\rho u_i' u_j'}$ is the turbulent flux, $\bar{p}$ is the thermodynamic pressure, ρ is the density of the fluid, and g is the gravity acceleration.

The Reynolds decomposition introduces Reynolds stress, which represents turbulence diffusive flux. The Boussinesq assumption, which states that the Reynolds stress is linearly proportional to the rate of strains, is made here to define the turbulent flux:

$$-\overline{\rho u_i' u_j'} = \mu_t\Big(\frac{\partial \bar{u}_i}{\partial x_j} + \frac{\partial \bar{u}_j}{\partial x_i}\Big) - \frac{2}{3}\delta_{ij}\Big(\mu_t\frac{\partial \bar{u}_k}{\partial x_k} + \rho k\Big), \quad (3)$$

where k is turbulence kinetic energy (TKE), μ_t is turbulence viscosity and would be yielded by solving auxiliary field equations of turbulence closure, which will be discussed in Section 2.2.

Gaseous substance is regarded as a passive scalar. The transport of a scalar can be modeled similarly. Turbulence transport of a scalar is taken to be proportional to the gradient of the mean value of the transported quantity. The unsteady-state form is applied here:

$$\frac{\partial \rho \overline{C}}{\partial t} + \frac{\partial(\rho \bar{u}_j \overline{C})}{\partial x_j} = \frac{\partial}{\partial x_j}(-\overline{\rho u_j' C'}) + S_C, \quad (4)$$

$$-\overline{\rho u_j' C'} = \Gamma_C \frac{\partial \overline{C}}{\partial x_j}, \quad (5)$$

where $\overline{C}$ is the mass fraction or mass concentration of a tracer, $\overline{\rho u_j' C'}$ is the turbulent flux of tracer, Γ_C is the turbulent diffusivity of tracer, and S_C is the source of mass of tracer.

The turbulent diffusivity, Γ_C, is expected fairly close to turbulence viscosity μ_t. The scale coefficient is defined as turbulent Schmidt number σ_C.

$$\sigma_C = \frac{\mu_t}{\Gamma_C}. \quad (6)$$

This assumption is known as the Reynolds analogy.

2.2 *Turbulence closure: the standard k-ε model*

The turbulence closure scheme applied here is widely used and can be referred to Launder and Spalding (1974).

The expression for the turbulence viscosity relates to TKE, k, and dissipation rate ε:

$$\mu_t = \frac{\rho C_\mu k^2}{\varepsilon}, \quad (7)$$

where C_μ is a constant.

For conditions of stationary, neutral, and high Reynolds number, the standard k-ε model equations for TKE, k, and dissipation rate ε are:

$$\frac{\partial(\rho \bar{u}_j k)}{\partial x_j} = \frac{\partial}{\partial x_j}\Big(\frac{\mu_t}{\sigma_k}\frac{\partial k}{\partial x_j}\Big) + G_k - \rho\varepsilon, \quad (8)$$

$$\frac{\partial(\rho \bar{u}_j \varepsilon)}{\partial x_j} = \frac{\partial}{\partial x_j}\Big(\frac{\mu_t}{\sigma_\varepsilon}\frac{\partial \varepsilon}{\partial x_j}\Big) + C_{1\varepsilon}\frac{\varepsilon}{k}G_k - C_{2\varepsilon}\rho\frac{\varepsilon^2}{k}, \quad (9)$$

with

$$G_k = \mu_i\Big(\frac{\partial \bar{u}_i}{\partial x_j} + \frac{\partial \bar{u}_j}{\partial x_i}\Big)\frac{\partial \bar{u}_i}{\partial x_j}, \quad (10)$$

where G_k is the production rate of TKE by shear stress, $C_{1\varepsilon}$ and $C_{2\varepsilon}$ are constants, σ_k and σ_ε are turbulent Prandtl numbers for k and ε respectively, and considered as constants too. Details about all these constants can be found in Launder and Spalding (1974).

2.3 *Wall boundary condition*

The above equations are used under high Reynolds number condition and are invalid in the near-wall regions, where Reynolds number is low and viscous stresses dominate the flow. Instead, uniform shear stress is assumed and wall functions are used in nodes adjacent to walls. Semi-empirical expressions (Launder and Spalding, 1974; Versteeg and Malalasekera, 2010) are used to relate to k, ε, and the friction velocity u_τ.

The implementation of wall boundary conditions in turbulence flow starts with the evaluation of two dimensionless parameters:

$$u^+ = \frac{\bar{u}}{u_\tau}, \quad (11)$$

$$y^+ = \frac{y\rho u_\tau}{\mu} = \frac{y}{\nu}\sqrt{\frac{\tau_w}{\rho}}, \quad (12)$$

where u_τ is friction velocity, τ_w is the wall shear stress, μ and ν are dynamic viscosity and kinematic viscosity coefficients, respectively, and y denotes distance to the wall.

Considering the situation with y^+ greater than 11.63 (Versteeg and Malalasekera, 2010), where the nodes adjacent to walls would be in the log-law region of a turbulence boundary layer:

$$u^+ = \frac{1}{\kappa}\ln(Ey^+). \quad (13)$$

In this formula, κ is von Karman's constant (= 0.4; Stull, 1988) and E is an integration constant. For smooth wall with constant shear stress, E has a value of 9.793 (Versteeg and Malalasekera, 2010).

The expressions to relate k, ε, and friction velocity u_τ are shown below:

$$k = \frac{u_\tau^2}{\sqrt{C_\mu}}, \tag{14}$$

$$\varepsilon = \frac{u_\tau^3}{\kappa y} = \frac{C_\mu^{3/4} k^{3/2}}{\kappa y}. \tag{15}$$

The expressions for wall shear stress τ_w and production of TKE are given as:

$$\tau_w = \rho C_\mu^{1/4} k^{1/2} u/u^+, \tag{16}$$

$$G_k = \tau_w \frac{\partial u}{\partial y}. \tag{17}$$

3. Numerical method

All equations are discretized using the finite-volume approach. The spatial discretization of all equations has adopted the hybrid differencing scheme upon control volumes of non-uniform cuboid shapes. The fully implicit scheme is used for time integration of concentration field. These nonlinear equations are solved by an iterative method named Semi-Implicit Method for Pressure-Linked Equations (SIMPLE). The brief description of SIMPLE algorithm is given below, and all detailed technologies except for that about the control volumes of non-uniform cuboid shapes are explained in Versteeg and Malalasekera (2010), as well as Wang (2004).

3.1 Finite volume method

Finite volume method is a special finite difference formulation that is central to the most well-established CFD codes: CFD/ANSYS, FLUENT, PHOENICS, and STAR-CD (Versteeg and Malalasekera, 2010). This method is based on the conservation property of physical variables, which makes it much easier to understand than the finite element and spectral methods do. The key step of the finite volume method is the integration of the transport equation over a three-dimensional control volume.

The steady equations for RANS and standard k-ε model can be derived from transport equation for a general property ϕ:

$$\frac{\partial(\rho \bar{u}_i \bar{\phi})}{\partial x_i} = \frac{\partial}{\partial x_i}\left[\Gamma_\phi \frac{\partial \bar{\phi}}{\partial x_i}\right] + S_\phi. \tag{18}$$

Formal integration over a control volume gives

$$\int_{\Delta V} \frac{\partial(\rho \bar{u}_i \bar{\phi})}{\partial x_i} \mathrm{d}V = \int_{\Delta V} \frac{\partial}{\partial x_i}\left[\Gamma_\phi \frac{\partial \bar{\phi}}{\partial x_i}\right] \mathrm{d}V + \int_{\Delta V} S_\phi \mathrm{d}V. \tag{19}$$

Figure 1 shows the schematic representation of the control volume adopted in our CFD model. Notation P denotes a general nodal point; notations N_i and L_i denote neighbor of node P in positive and negative i-direction, respectively; notations n_i and l_i denote side faces of control volume of node P in positive and negative i-direction, respectively; $\Delta x_{i,P}$ is referred to as control volume width in i-direction for node P; the distances between nodes P and N_i, and between nodes P and L_i are identified by δx_{PN_i} and δx_{PL_i} respectively; similarly distances between point P and face n_i, and between point P and face l_i are denoted by δx_{Pn_i} and δx_{Pl_i}, respectively.

In the control volume shown in Fig. 1, Eq. (19)

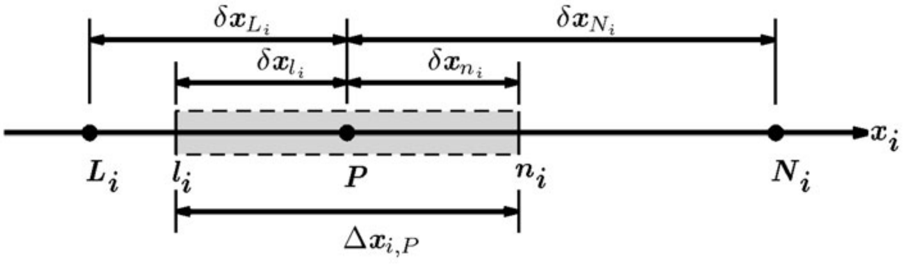

Fig. 1. Schematic representation of the control volume.

can be reformatted as

$$\sum_i (\rho\bar{u}_i A\bar{\phi})_{n_i} - (\rho\bar{u}_i A\bar{\phi})_{l_i} = \sum_i \Big(\Gamma_\phi A\frac{\partial\bar{\phi}}{\partial x_i}\Big)_{n_i} - \Big(\Gamma_\phi \frac{\partial\bar{\phi}}{\partial x_i}\Big)_{l_i} + \overline{S}_\phi \Delta V, \tag{20}$$

where A is the area of side face, and $\overline{S}_\phi$ is the average of source strength in the control volume.

3.2 Hybrid differencing scheme

In order to derive useful forms of the discretized equations, the properties at the interface n_i and l_i in Eq. (20) are required. Many schemes can deal with the interface properties, but the central differencing scheme seems a simple and reliable way of calculating interface values and the gradients because it uses linear approximations and is second-order accurate. However, it would fail when convection is much stronger than diffusion. The upwind scheme, which determines the interface values (not gradients) only by the upwind values, is another simple approach. Although it is absolutely stable, it has only first-order accuracy. To avoid these defects, we adopt the hybrid differencing scheme, a method that has combined advantages of central and upwind differencing schemes.

Define convective mass flux $F = \rho\bar{u}$ and diffusion conductance $D = \dfrac{\Gamma_\phi}{\delta x}$ at the interface. We employ the central differencing approach to the diffusion term in Eq. (20), no matter what scheme is used for convective term. Equation (20) turns out to be:

$$\sum_i F_{n_i} A_{n_i}\bar{\phi}_{n_i} - F_{l_i} A_{l_i}\bar{\phi}_{l_i} = \sum_i D_{n_i} A_{n_i}(\bar{\phi}_{N_i} - \bar{\phi}_P) - D_{n_i} A_{l_i}(\bar{\phi}_P - \bar{\phi}_{L_i}) + \overline{S}_\phi \Delta V. \tag{21}$$

Here, it should be noted that $A_{n_i} = A_{l_i}$ in our model.

In order to apply control volumes of non-uniform cuboid shapes, we deduce the discretized equations from the uniform ones of Versteeg and Malalasekera (2010) and Wang (2004). We define the interpolation coefficient as $c_{n_i} = \dfrac{\delta x_{Pn_i}}{\delta x_{PN_i}}$ and $c_{l_i} = \dfrac{\delta x_{Pl_i}}{\delta x_{PL_i}}$ for n_i and l_i side faces, respectively.

Define non-dimensional cell Peclet number, $P_e = \dfrac{F}{D}$, as a measure of the relative strength of convection and diffusion. The hybrid differencing scheme employs the central differencing scheme when $|P_e| < 1/c$ (c is interpolation coefficient defined above) and the upwind differencing when $|P_e| \geqslant 1/c$. The final steady transport equation deduced with the finite volume method and hybrid differencing scheme is given as:

$$a_P\bar{\phi}_P = \sum_i (a_{N_i}\bar{\phi}_{N_i} + a_{L_i}\bar{\phi}_{L_i}) + \overline{S}_\phi \Delta V, \tag{22}$$

where

$$a_{N_i} = \max\big[-F_{n_i}\cdot A_{n_i}, (D_{n_i} - c_{n_i}F_{n_i})\cdot A_{n_i}, 0\big], \tag{23a}$$

$$a_{L_i} = \max\big[F_{l_i}\cdot A_{l_i}, (D_{l_i} + c_{l_i}F_{l_i})\cdot A_{l_i}, 0\big], \tag{23b}$$

$$a_P = \sum_i a_{N_i} + a_{L_i}. \tag{23c}$$

Here, it is noticed that the second column in the right side of Eq. (23) denotes the central differencing scheme.

3.3 Fully implicit time scheme

The fully implicit scheme is used for time integration of the concentration field, because it is unconditionally stable for any length of the time step.

The unsteady form of transport equation integrated over a small interval Δt from t to $t + \Delta t$ in a control volume is

$$\int\limits_{\Delta t}\int\limits_{\Delta V} \rho\bar{\phi}\mathrm{d}V\mathrm{d}t + \int\limits_{\Delta t}\int\limits_{\Delta V} \frac{\partial(\rho\bar{u}_i\bar{\phi})}{\partial x_i}\mathrm{d}V\mathrm{d}t = \int\limits_{\Delta t}\int\limits_{\Delta V} \frac{\partial}{\partial x_i}\Big[\Gamma_\phi\frac{\partial\bar{\phi}}{\partial x_i}\Big]\mathrm{d}V\mathrm{d}t + \int\limits_{\Delta t}\int\limits_{\Delta V} S_\phi \mathrm{d}V\mathrm{d}t. \tag{24}$$

Under the fully implicit time scheme, Eq. (24) can be rewritten as:

$$\Big(\int\limits_{\Delta V}\rho\bar{\phi}\mathrm{d}V\Big)\Big|_{t+\Delta t} - \Big(\int\limits_{\Delta V}\rho\bar{\phi}\mathrm{d}V\Big)\Big|_{t} + \Big[\int\limits_{\Delta V}\frac{\partial(\rho\bar{u}_i\bar{\phi})}{\partial x_i}\mathrm{d}V\Big]\Big|_{t+\Delta t}\cdot\Delta t = \Big(\int\limits_{\Delta V}\frac{\partial}{\partial x_i}\Big(\Gamma_\phi\frac{\partial\bar{\phi}}{\partial x_i}\Big)\mathrm{d}V\Big)\Big|_{t+\Delta t}\cdot\Delta t + \Big(\int\limits_{\Delta V}S_\phi\mathrm{d}V\Big)\Big|_{t+\Delta t}\cdot\Delta t. \tag{25}$$

3.4 SIMPLE algorithm

The Semi-Implicit Method for Pressure-Linked Equations (SIMPLE) is essentially a guess-and-correct procedure for the calculation of pressure.

A pressure field p^* is guessed to initiate the SIMPLE calculation process. Discretized momentum equations are solved using the guessed pressure field to yield velocity components $\bar{u}_i^*$ as follows:

$$\begin{aligned} a_{i,P}\bar{u}_{i,P}^* = &\sum_j \left(a_{i,N_j}\bar{u}_{i,N_j}^* + a_{i,L_j}\bar{u}_{i,L_j}^*\right) \\ &+ \left(p_{l_i}^* - p_{n_i}^*\right) \cdot A_{i,P} + b_{i,P}. \end{aligned} \tag{26}$$

Notice that Eq. (26) is obtained by replacing $\bar{\phi}$ with $\bar{u}_i^*$ and extracting the pressure gradient force from the source term in Eq. (22). The variable $A_{i,P}$ is area of side face in i-direction, and $b_{i,P}$ is the remaining source term.

The guessed pressure field p^* needs to be corrected. Define the correction p' as the difference between true pressure field p and the guessed pressure field p^*, so $p = p^* + p'$. Similarly, define velocity correction $\bar{u}_i'$, which satisfies $\bar{u}_i = \bar{u}_i^* + \bar{u}_i'$.

The true fields p and $\bar{u}_i$ also satisfy the transport equation (Eq. (26)). Substitution of the transport equations of true field and guessed field yields the correction of velocity field:

$$\begin{aligned} a_{i,P}\bar{u}_{i,P}' = &\sum_j \left(a_{i,N_j}\bar{u}_{i,N_j}' + a_{i,L_j}\bar{u}_{i,L_j}'\right) \\ &+ \left(p_{l_i}' - p_{n_i}'\right) \cdot A_{i,P}. \end{aligned} \tag{27}$$

Equation (27) implies that the remaining source term maintains the same between the true field and guessed field.

Since neglecting the term $\sum\limits_j \left(a_{i,N_j}\bar{u}_{i,N_j}' + a_{i,L_j}\bar{u}_{i,L_j}'\right)$ would not change the final convergence value, SIMPLE algorithm omits these terms to simplify Eq. (27) and obtain the correction formula for guessed velocity field:

$$\bar{u}_{i,P}' = d_{i,P}\left(p_{l_i}' - p_{n_i}'\right), \tag{28}$$

with $d_{i,P} = \dfrac{A_{i,P}}{a_{i,P}}$.

To complete the correction, correction p' is needed. The velocity field is also subject to the constraint of continuity equation, which replaces $\bar{\phi}$ with number 1 and sets the source term to zero in Eq. (20) or Eq. (22). With $\bar{u}_i = \bar{u}_i^* + \bar{u}_i'$ and Eq. (28), the equation for p' can be deduced from continuity equation:

$$a_P' p_P' = \sum_i \left(a_{N_i}' p_{N_i}' + a_{L_i}' p_{L_i}'\right) + b_P', \tag{29}$$

where

$$a_{N_i}' = \rho A_{i,P}(d_{i,P})_{\bar{u}_{i,n_i}'}, \tag{30a}$$

$$a_{L_i}' = \rho A_{i,P}(d_{i,P})_{\bar{u}_{i,l_i}'}, \tag{30b}$$

$$a_P' = \sum_i (a_{N_i}' + a_{L_i}'), \tag{30c}$$

$$b_P' = \sum_i \left[\rho_{l_i}\bar{u}_{i,l_i}^* - \rho_{n_i}\bar{u}_{i,n_i}^*\right] \cdot A_{i,P}. \tag{30d}$$

The notation $(d_{i,P})_{\bar{u}_i'}$ denotes the coefficient $d_{i,P}$ of $\bar{u}_i'$ when solving Eq. (28).

The whole iteration procedure of SIMPLE algorithm used in our model is given in Fig. 2.

4. Results and discussion

In order to validate the proposed numerical mo-

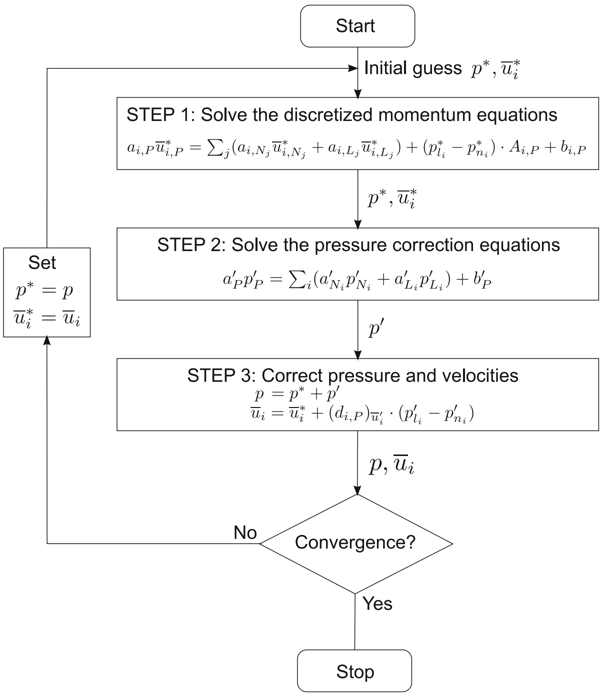

Fig. 2. The SIMPLE algorithm.

del, simulations of dispersion sources release, which are expected to reproduce the wind tunnel experiments, have been carried out. Three datasets from the Compilation of Experimental Data for Validation of Microscale Dispersion Models (CEDVAL) provided by the Environmental Wind Tunnel Laboratory in University Hamburg are used in this study. The datasets are chosen because all the experiments were well organized and clearly documented, and the datasets are fully accessible at http://www.mi.uni-hamburg.de/Data-Sets.432.0.html. These wind tunnel experiments were carried out at a scale of 1:200 in the BLASIUS wind tunnel at the Meteorological Institute of the University of Hamburg. The first two corresponded to detailed measurements of the flow and dispersion characteristics around an isolated rectangular obstacle, respectively, and the third one corresponded to array of obstacles. Dynamic similarity was maintained between simulations and wind tunnel experiments.

4.1 Simulation setup

Urban areas with densely built-up landuse would significantly affect the local atmospheric condition, such as the airflow field and air quality, so it is necessary to evaluate the dynamic effects of buildings. On the other hand, for the purpose of validating a newly built numerical model, numerical simulations for simple cases are appropriate, because the factors which influence the experiments are fewer and easier to control and to evaluate. In this study, the first numerical validation case was performed for an isolated rectangular obstacle.

The A1-1 and A1-5 data of CEDVAL were selected to validate the simulations of isolated obstacle. Although the A1-1 and A1-5 data belong to different experiments, they share the same experimental parameters, including roughness length (= 7×10^{-4} m), friction velocity (= 0.377 m s^{-1}), obstacle size (= 100 mm×150 mm×125 mm) and so forth. The difference between these two datasets is the type of measured data: the A1-1 dataset contains the measured data of flow characteristics and the A1-5 dataset contains the measured data of dispersion.

In this case, two simulations were set up to correspond to A1-1 and A1-5 data, respectively. These simulations applied the real scale (H=25 m). Table 1 and Fig. 3 show detailed parameters and a schematic representation of the computational domain and mesh used. The setup sketch of the single obstacle and sources is available at http://www.mi.uni-hamburg.de/fileadmin/files/forschung/techmet/physmod/cedval/datafiles/A1-5/A1-5-SS-1.GIF. The sources were released continuously and constantly. Because the concentration in this study is defined in a dimensionless form, the source strength can be prescribed as any value and is omitted in this paper. The default turbulent Schmidt number for diffusion of tracer, σ_C, is set to 1, because of no implication for this value in measured data. The domain was extended up to a large distance in three directional axes to ensure that zero gradient assumption is rational along the lateral, outlet, and top boundaries. At the inlet boundary, velocity components $\bar{v}$ (y-direction) and $\bar{w}$ (z-direction) are considered to be equal to zero and the wind velocity and TKE profiles are provided according to the measured data.

The second case is considered for a little more complex situation with an array of obstacles, which stands for an extremely orderly city block. It is a well-organized group of buildings and also a common element in an urban area. Still this case is not too

Table 1. Numerical grids for the simulation conducted in this study

Parameter (unit)	Symbol	Isolated obstacle simulations	Obstacle array simulations
Grid points	$N_x \times N_y \times N_z$	92×84×47	139×76×38
Length scale (m)	H	25	25
Domain size (H)	$L \times W \times Z$	18.4×19.1×7.4	41.2×25.0×9.1
Obstacle size (H)	$l \times w \times h$	0.8×1.2×1.0	0.8×1.2×1.0
Horizontal grid spacing (H)	$\Delta x,\ \Delta y$	0.025–1	0.056–1
Vertical grid spacing (H)	Δz	0.012–1	0.02–1
Time step of dispersion (s)	Δt	0.05	0.05

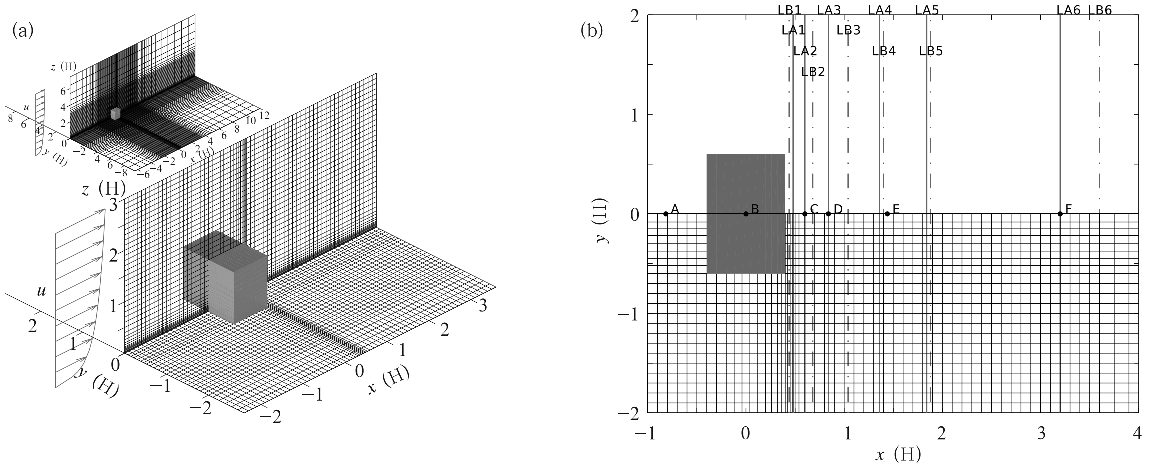

Fig. 3. Schematic representation of isolated rectangular obstacle simulation domain: (a) mesh used for the computational simulations (the whole area is shown in the insert) and (b) positions of comparisons between simulation results and measured data. The points and lines indicate the positions for the validation in Section 4.2.

complex for the same reason. The B1-1 dataset of CEDVAL, which contains measured data of both flow and dispersion, was selected to validate the simulation of array of obstacles. This dataset also shares the same experimental parameters and the same-size obstacles. The simulation setup adopted the same principle of the isolated rectangular obstacle simulation. Table 1 and Fig. 4 show detailed parameters and a schematic representation of the computational domain and mesh, respectively. The 3×7 array of rectangular obstacles (Fig. 4) is applied in this simulation and the obstacles have exactly the same dimension as that in simulation of isolated obstacle. The sources are set up at the leeward side of the building at origin (x/H=0, y/H=0),

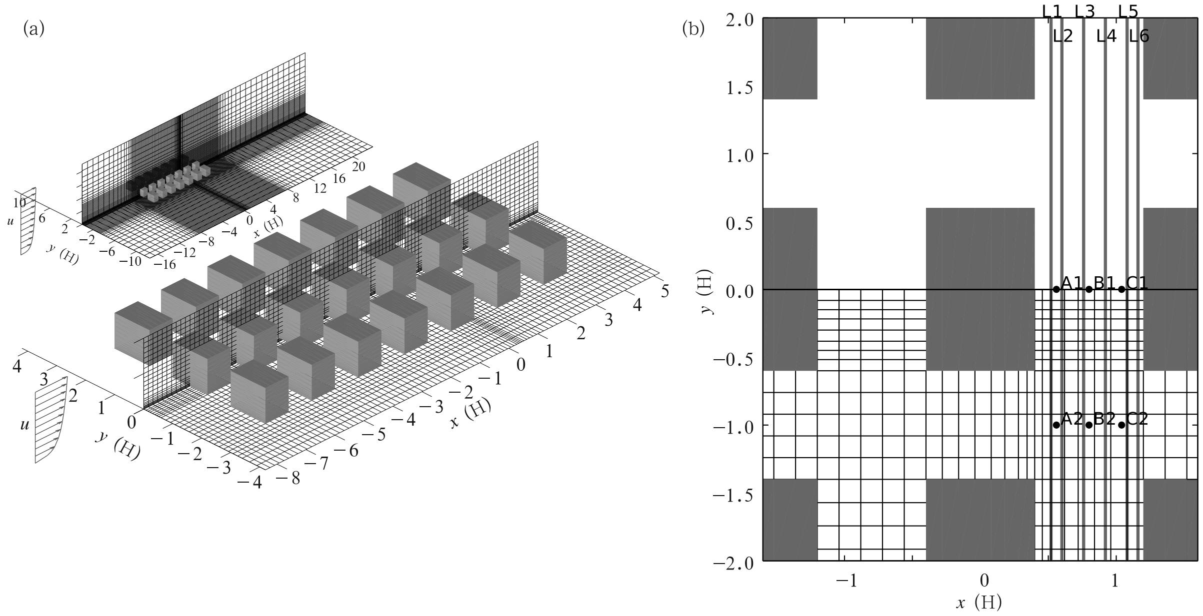

Fig. 4. Schematic representation of the array of rectangular obstacles and the simulation domain: (a) mesh used for the computational simulations (the whole area is shown in the insert) and (b) positions of comparisons between simulation results and measured data. The points and lines indicate the positions for the validation in Section 4.3.

which is shown in the setup sketch of the sources.

4.2 Validation of the isolated rectangular obstacle simulations

Figure 5 shows the streamline of velocity around the isolated obstacle. It is found that the mean flow impinging the windward face of the obstacle is decelerated rapidly and part of the momentum in the main direction is transferred to the spanwise and vertical momentum. Streamline deflects and separates from the horizontal plane (Fig. 5b), and the flow is driven into vertical downward and upward. The downward part creates a reverse flow extending to about 0.4H in front of the lower half height of the obstacle (Fig. 5b), reattaches on its front face, and generates the horseshoe vortex (Fig. 5b). The upward part flow separates at the sharp leading edge and then reattaches to the roof of the obstacle, and separates again at the downwind edge (Fig. 5b). Similar behavior is also found at the sides of the obstacle (Fig. 5a). The separated flow passes over the building, and reattaches on the ground further downwind at about 1.4H after the leeward side of the obstacle (Fig. 5b). The flow comes from the flow adjacent to the roof and lateral side of the obstacle travels upstream at the reattaching point and results in the formation of a recirculation region behind the obstacle (Figs. 5a and 5b).

The TKE field is given in Fig. 6. Values of the TKE close to corners of the building front walls are the highest (Fig. 6b), which results from the extremely high wind velocity gradient. On the roof and the lateral sides of the obstacle, the TKE values are also much higher than that of the free flow because of the high wind velocity gradients there. In the recirculation region, though the values of the TKE are not as high as that close to the corners, the values are higher than those on the roof and side of the obstacle. In the downstream region of recirculation, which is about 4H after the leeward side of the obstacle, the turbulence levels are still slightly higher than those in the free flow, which proves that the flow is still disturbed by the obstacle.

Comparison of the computed and measured velocity is shown in Fig. 7. The velocities are non-dime-

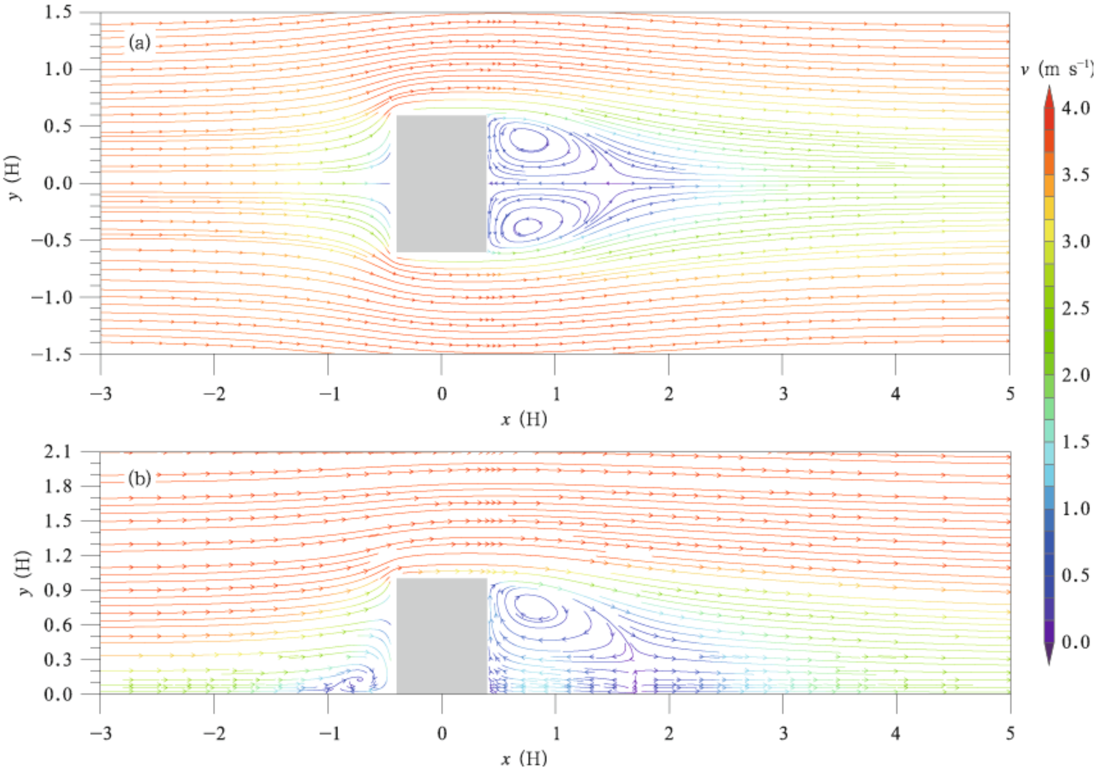

Fig. 5. Computational streamline of isolated obstacle at (a) $z/H = 0.5$ (plan view) and (b) $y/H = 0$ (side view).

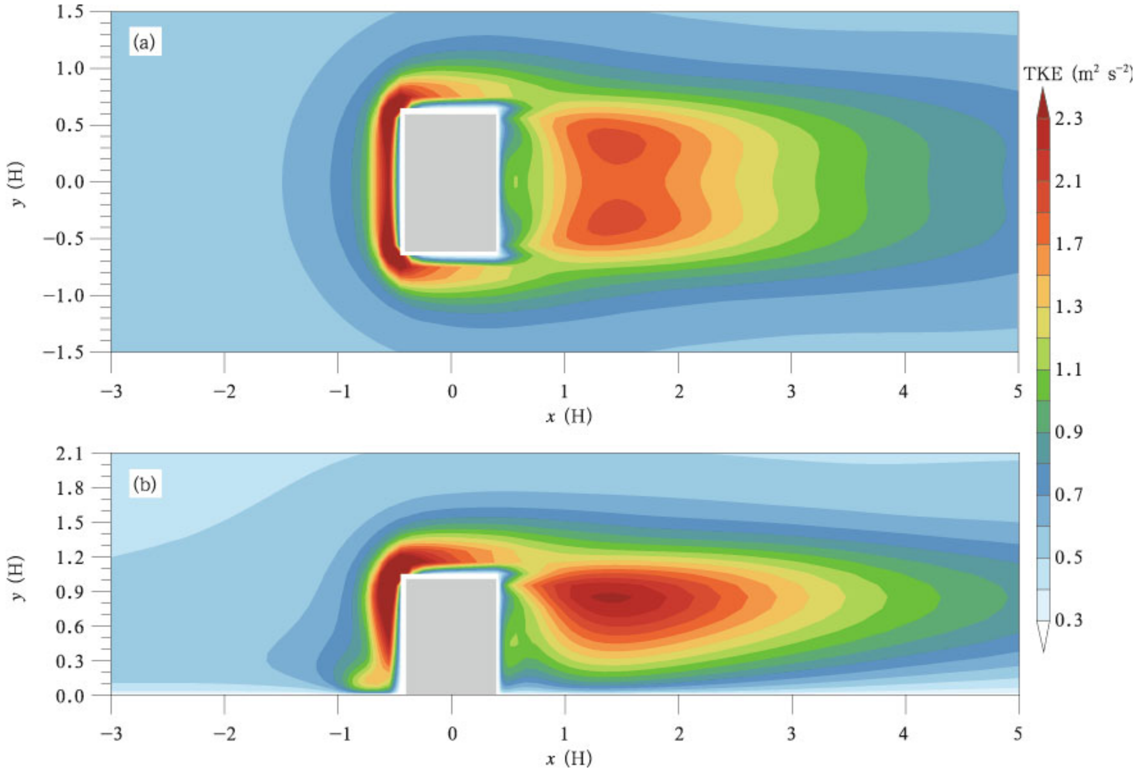

Fig. 6. Computational TKE contours of isolated obstacle at (a) $z/H = 0.5$ (plan view) and (b) $y/H = 0$ (side view).

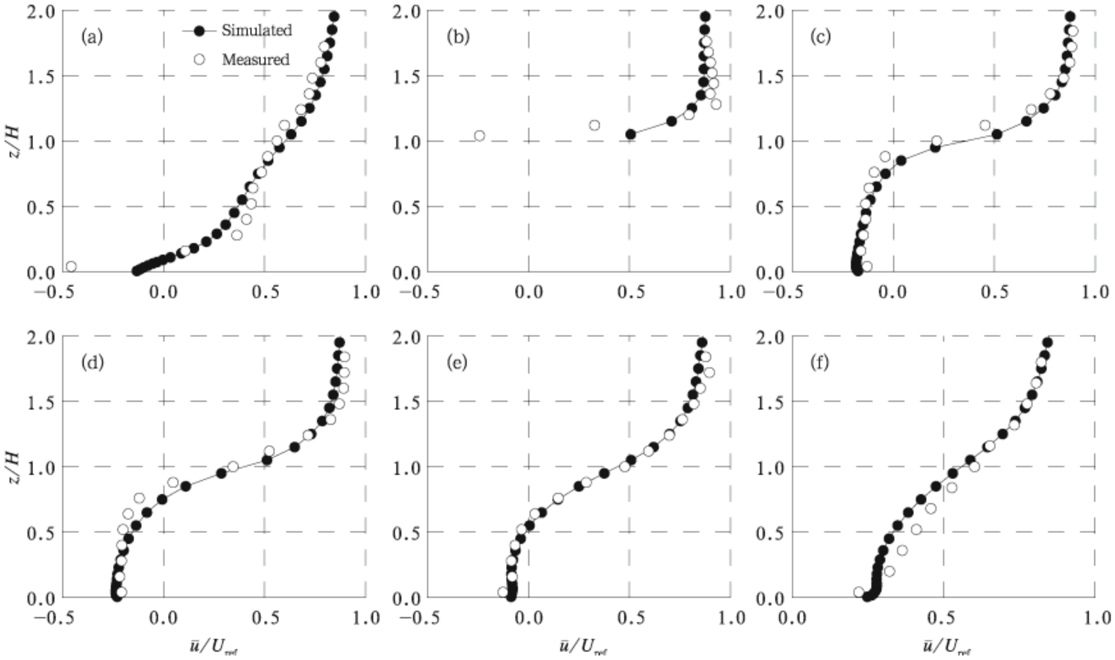

Fig. 7. Streamwise velocity from experimental data (unfilled circles) and simulation (filled circles and lines) of (a) A ($x/H = -0.816$, $y/H = 0$), (b) B ($x/H = 0$, $y/H = 0$), (c) C ($x/H = 0.6$, $y/H = 0$), (d) D ($x/H = 0.84$, $y/H = 0$), (e) E ($x/H = 1.44$, $y/H = 0$), and (f) F ($x/H = 3.2$, $y/H = 0$) in the case of an isolated obstacle.

nsionalized by the reference velocity at the height of 4H. The velocity profiles appear to be predicted reasonably well, especially in Figs. 7a and 7c–f. In Fig. 7b, the measured velocity adjacent to the roof is negative, while the computational velocity is not, which indicates that the model under-predicts the separation intensity of the flow on the roof.

Comparison of the computed and measured TKE is given in Fig. 8. The data of velocity fluctuations in spanwise (y) direction at the center plane ($y = 0$) are unavailable in A1-1 dataset. The sum of velocity fluctuations in streamwise (x) and vertical (z) directions instead of complete TKE are used here. The Reynolds stress tensor in Eq. (3) is used to predict the velocity fluctuations. Although the general trend of predicted TKE is not as good as that of wind field, the shape and peak locations of the turbulence field are well predicted. At the location of long distance from the leeward side of the obstacle (Figs. 8e and 8f), the model predicts the TKE much better in both the shape and peak value. Figure 8b shows a large difference between the measured peak value and the simulated one on the roof. The measured peak value is over three times as much as the simulated one. The reason may be the underestimation of the velocity gradient due to underprediction of the separation intensity of the flow on the roof (Fig. 7b).

The concentration has been non-dimensionalized by using the following equation:

$$K_c = \frac{\overline{C}U_{\mathrm{ref}}H^2}{C_sQ}, \tag{31}$$

where $\overline{C}$ is the mean concentration, U_{ref} is the mean wind speed at reference height, which is 5.28H in this case, C_s is the tracer concentration in the sources, and Q is the total volumetric flow rate of the gas source.

The concentration field after the time when it reaches equilibrium is chosen to validate.

In Sections 4.2 and 4.3, only experimental data (unfilled circles) and simulation with non-corrected turbulent Schmidt number (filled circles and solid lines) are used for discussion. The simulation with corrected turbulent Schmidt number (dashed lines) will be discussed in Section 4.4 exclusively.

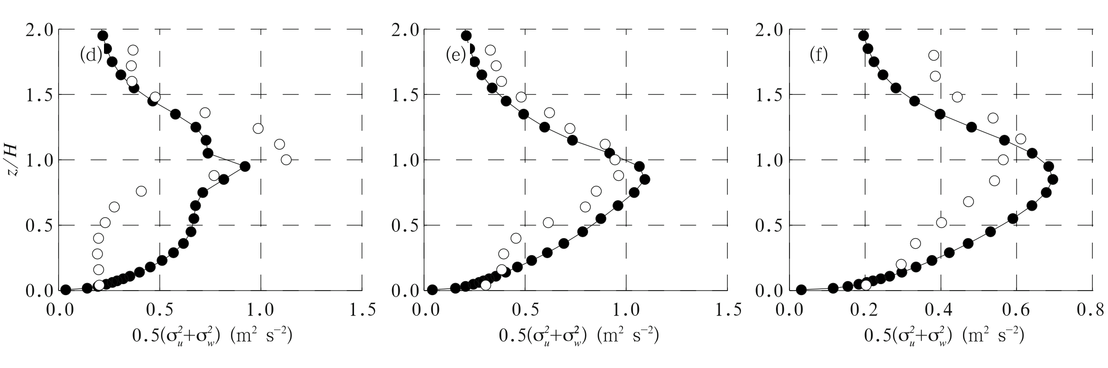

Fig. 8. As in Fig. 7, but for velocity fluctuations.

Comparison of the computed and measured concentration is shown in Figs. 9 and 10. Although the overall tendency of the model is to under-predict the spread and overestimate the peak values, the shape and peak locations are well predicted.

4.3 Validation of the rectangular obstacle array simulations

The simulated wind fields are shown in Fig. 11. Even when an array of obstacles are present, general characteristics of the wind field are quiet similar to

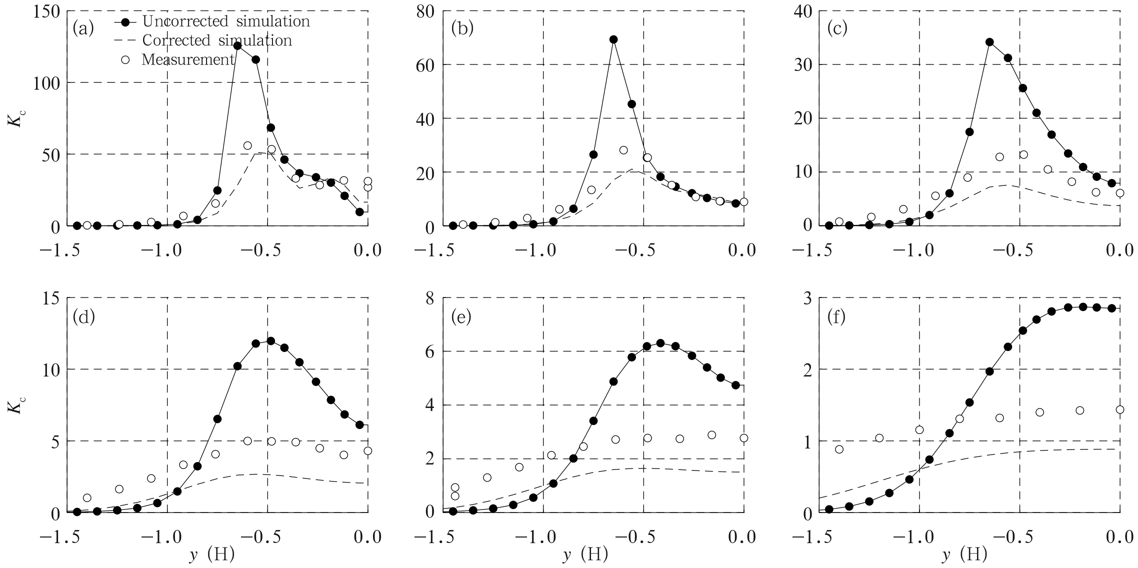

Fig. 9. Dimensionless concentration in spanwise (y) direction of line (a) LA1 ($x/H = 0.48$), (b) LA2 ($x/H = 0.60$), (c) LA3 ($x/H = 0.84$), (d) LA4 ($x/H = 1.36$), (e) LA5 ($x/H = 1.84$), and (f) LA6 ($x/H = 3.2$) at $z/H = 0.08$ in the case of an isolated obstacle. Results from the experimental data (unfilled circles), the simulation with non-corrected turbulent Schmidt number (solid curves with filled circles), and the simulation with corrected turbulent Schmidt number (dashed curves) are shown in each panel.

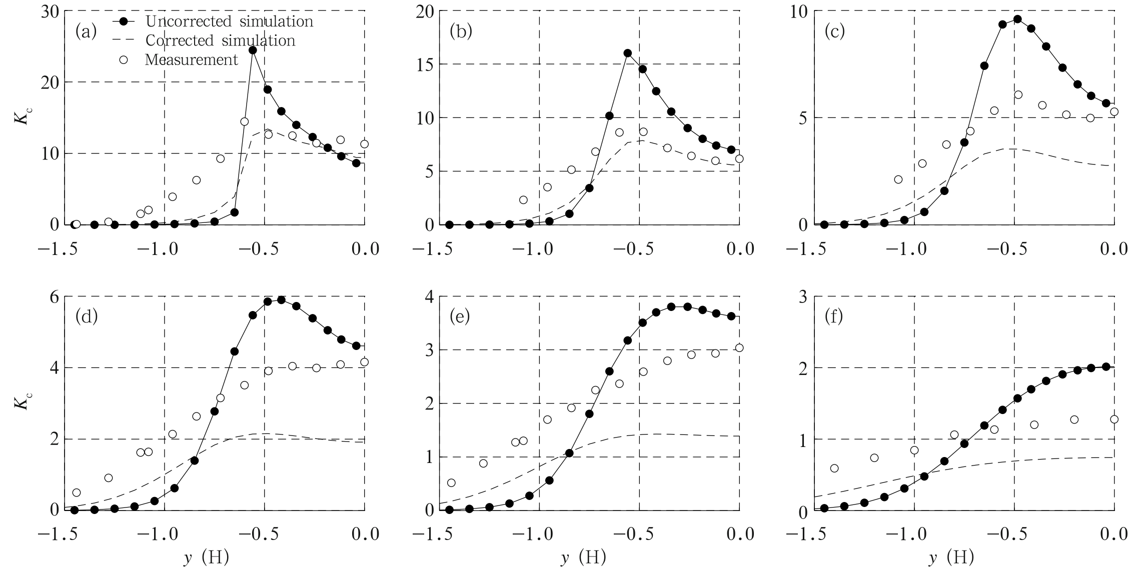

Fig. 10. As in Fig. 9, but of line (a) LB1 ($x/H = 0.44$), (b) LB2 ($x/H = 0.68$), (c) LB3 ($x/H = 1.04$), (d) LB4 ($x/H = 1.40$), (e) LB5 ($x/H = 1.88$), and (f) LB6 ($x/H = 3.60$) at $z/H = 0.28$.

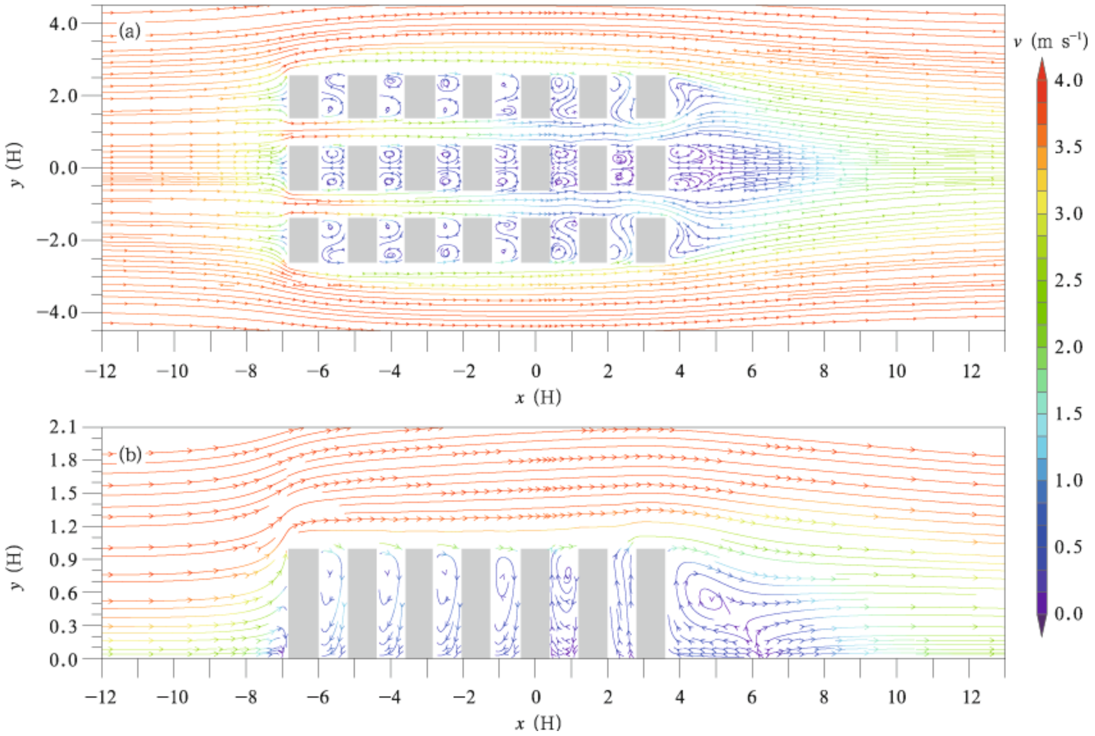

Fig. 11. Computational streamline around the array of obstacles at (a) $z/H = 0.5$ (plan view) and (b) $y/H = 0$ (side view).

those in Fig. 5 in the impinging region. The reverse region extends to about 0.2H in front of the first column of obstacles (Fig. 11b). However, the recirculation region shows something different. The recirculation region extending to about 2.7H after the last column of obstacles only appears after the middle row of the obstacles (Fig. 11a). The flow that wraps the lateral sides of the whole array only reattaches further downwind and does not travel upstream to form a recirculating flow. Within the array of the obstacles, the velocity decreases as the column number of the obstacles increases (in the positive i-direction). The recirculating flow appears in each region between any two obstacles in the streamwise (x) direction.

The simulated turbulence fields are shown in Fig. 12. The general turbulence field wrapping the whole array of obstacles is also similar to that in Fig. 6. Within the array, the values of TKE maintain highly close to top corners of the obstacle front walls (Fig. 12b), although the values there decrease with the increasing column number. In the channel between two rows of obstacles and the recirculation region between two columns (Fig. 12a), the values of TKE also decrease as the column number increases. Some values of TKE in the regions near the last column are even lower than those in the free flow. This is due to the decreasing of the wind velocity gradients caused by the reduction of wind velocity within the array along the streamwise direction (Fig. 11).

Comparison of the simulated and measured velocity is shown in Fig. 13. The velocity field appears to be predicted well in general. The prediction of the streamwise velocity above the obstacle height H is better than that below it. At the center plane (Figs. 13a–c), prediction of the velocity underestimates the wind speed below about 0.3H, resulting in the underestimation of the intensity of the recirculation flow. At the plane of $y/H = -1$ (Figs. 13d–f), the prediction turns out to under-predict the wind speed below the obstacle height.

Comparison of the simulated and measured TKE is shown in Fig. 14. Although the general prediction of TKE is not as good as that of wind field, the TKE field shape and peak locations are also predicted rati-

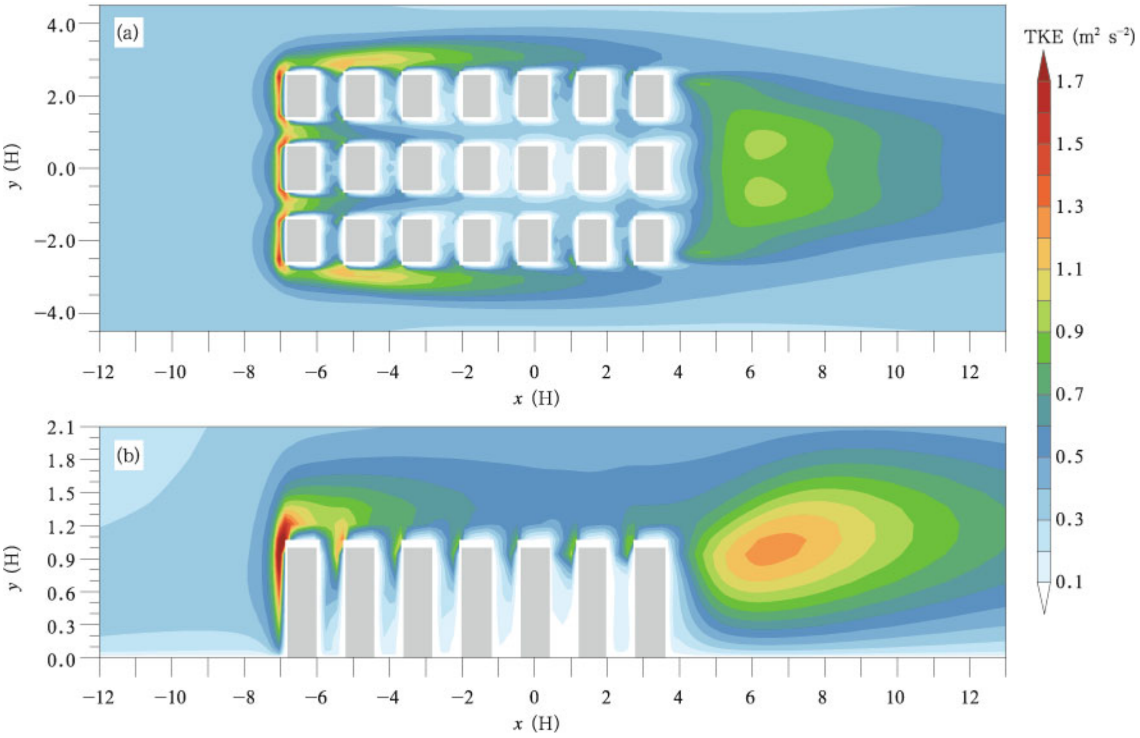

Fig. 12. Computational TKE contours around the array of obstacles at (a) $z/H = 0.5$ (plan view) and (b) $y/H = 0$ (side view).

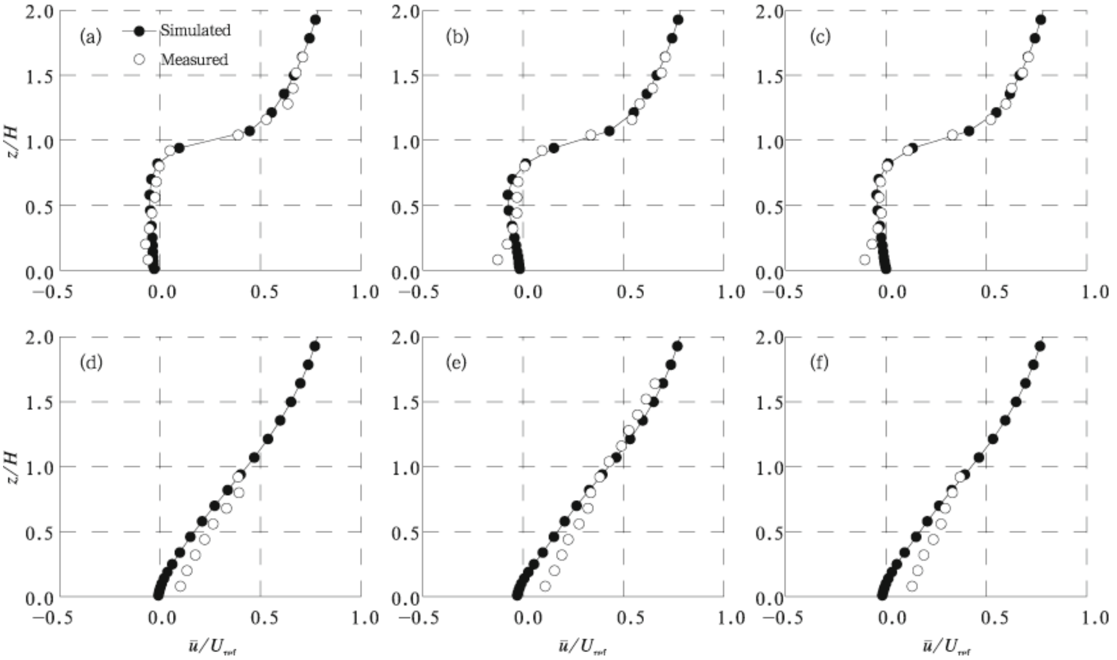

Fig. 13. Streamwise velocity from the experimental data (unfilled circles) and simulation (filled circles) of (a) A1 ($x/H = 0.56$, $y/H = 0$), (b) B1 ($x/H = 0.8$, $y/H = 0$), (c) C1 ($x/H = 1.04$, $y/H = 0$), (d) A2 ($x/H = 0.56$, $y/H = –1$), (e) B2 ($x/H = 0.8$, $y/H = –1$), and (f) C2 ($x/H = 1.04$, $y/H = –1$) in the case of an array of obstacles.

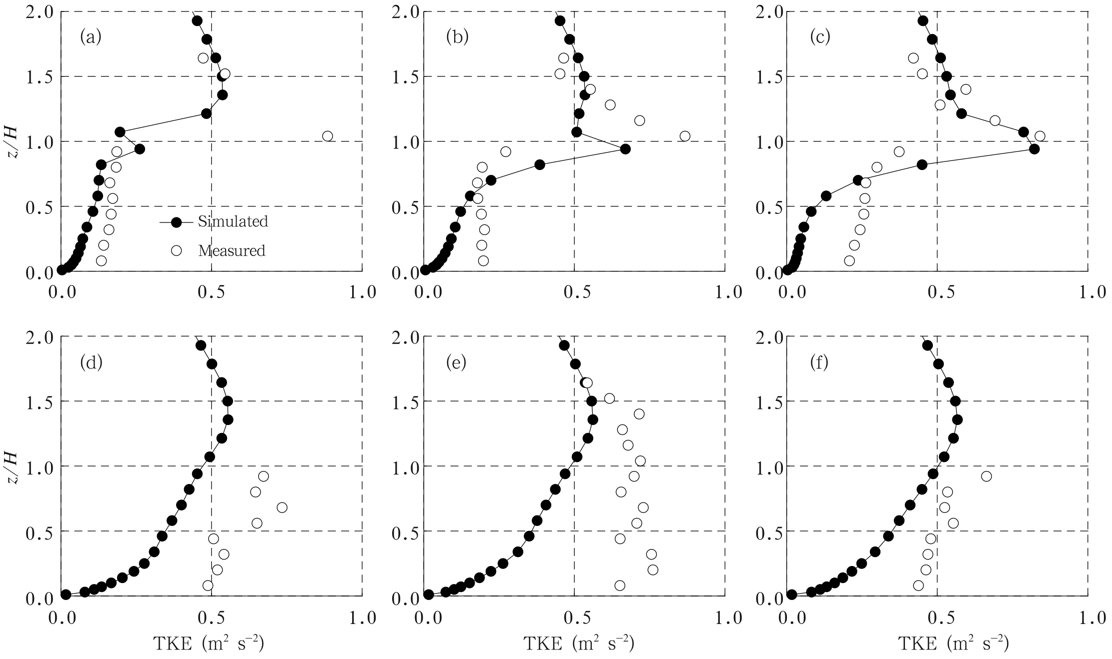

Fig. 14. As in Fig. 13, but for TKE.

onally well. At the center plane (Figs. 14a–c), the model tends to under-predict the values of TKE below the obstacle height, while the simulation shows a better agreement with the observation above that height. At the plane of $y/H = -1$ (Figs. 14d–f), the model under-predicts the entire TKE profiles, especially in the region near surface.

Comparison of the simulated and measured concentration is shown in Fig. 15. The concentration has also been non-dimensionalized by using Eq. (31). The concentration field shape and peak locations are also well predicted in the simulation. While the spread of the concentration field near leeward side (Figs. 15a and 15b) of the source building appears to be under-predicted, the peak value is over-predicted. In the middle (Figs. 15c and 15d) of the source building and the building behind, both the spread and the peak values are under-predicted, while near windward side (Figs. 15e and 15f) of the building behind, the model predicted the concentration well both in the spread and peak values.

4.4 Discussion about the turbulent Schmidt number

Clearly, the simulations have underestimated dispersal ability of the tracer. This may result from the improper turbulent Schmidt number (σ_C= 1) for the tracer in the model. Flesch et al. (2002) reported that the turbulent Schmidt number could range from 0.17 to 1.34. Other studies (Koeltzsch, 2000; Tominaga and Stathopoulos, 2007) also suggested different values of turbulent Schmidt number in a large range. Therefore, it is necessary to determine a proper value for our simulations.

The correction used here is based on the measured dimensionless tracer concentration in the wind tunnel experiment and the simulation with non-corrected turbulent Schmidt number. The correction will be obtained by adopting some assumptions from the Gaussian plume model. It is emphasized hereby that: as mentioned in Section 1, the Gaussian plume model is not comprehensive enough to be applied to an urban area; thus, our correction would not come from the area that is strongly disturbed by the building. The detailed selections would be shown after the deduction of the correction factor.

Define the correction factor

$$\gamma = \frac{\sigma_{Cm}}{\sigma_{Cs}}, \tag{32}$$

where σ_{Cm} is the corrected turbulent Schmidt number

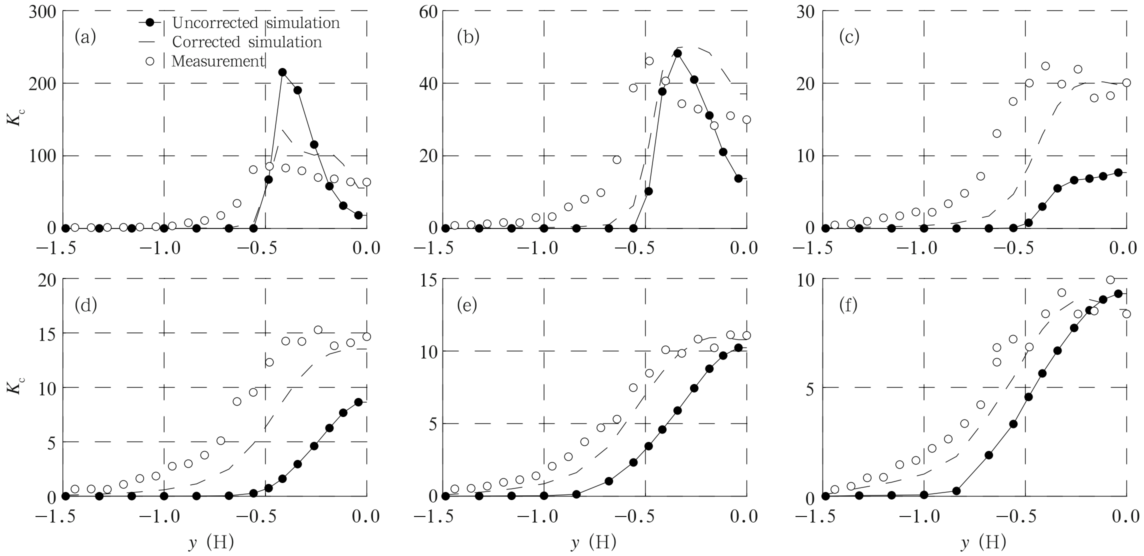

Fig. 15. Dimensionless concentration in spanwise (y) direction of line (a) L1 (x/H = 0.52), (b) L2 (x/H = 0.60), (c) L3 (x/H = 0.76), (d) L4 (x/H = 0.92), (e) L5 (x/H = 1.08), and (f) L6 (x/H = 1.16) at z/H = 0.06 in the case of an array of obstacles. Results from the experimental data (unfilled circles), the simulation with non-corrected turbulent Schmidt number (filled circles and solid curves), and the simulation with corrected turbulent Schmidt number (dashed curves) are shown in each panel.

of tracer and σ_{Cs} is the non-corrected turbulent Schmidt number of tracer.

In the Gaussian plume model with Taylor's frozen turbulence hypothesis, the turbulent diffusivity can be obtained following the formula (Sykes and Gabruk, 1997) below:

$$\sigma_y^2 = 2\int \Gamma_C \mathrm{d}t, \tag{33}$$

where σ_y is the standard deviation of displacement of tracer in spanwise (y) direction.

Combining Eq. (6) with Eq. (32), γ can be rewritten as below:

$$\gamma = \frac{\sigma_{ys}^2}{\sigma_{ym}^2}, \tag{34}$$

where σ_{ys} is the standard deviation of displacement of simulation and σ_{ym} is the standard deviation of displacement of observational data.

Figures 9 and 10 show that the simulations using the non-corrected dimensionless concentration in spanwise direction have a symmetrical shape with two peaks. In this study, we assume that the dimensionless concentration in the region far enough from the area where the flow is strongly disturbed by the obstacle, corresponds to a Gaussian plume diffusion model assumption with two symmetrical point sources. The formula is superposition of two symmetrical Gaussian distributions:

$$K_C(y) = \frac{Q_{K_C}}{\sqrt{2\pi}\sigma_y}\Big(\mathrm{e}^{-\frac{(y-y_0)^2}{2\sigma_y^2}} + \mathrm{e}^{-\frac{(y+y_0)^2}{2\sigma_y^2}}\Big). \tag{35}$$

This assumption of two sources is rational, because symmetrical recirculation regions shown in Fig. 5 tend to mix the tracer in each region and form two symmetrical sources.

The correction factor was obtained from the measured and simulated results of the isolated obstacle. In order to ensure the above Gaussian plume model's assumption can be satisfied as much as possible, we avoided use of the data that came from the region strongly affected by the obstacle. Data beyond x/H= 2 seemed a reasonable choice, since the region of $x/H \geqslant 2$ was after the recirculation region caused by the obstacle. The fitting values of σ_{ys} and σ_{ym} are shown in Table 2.

Table 2. The fitting standard deviation of displacement in spanwise (y) direction of the simulation and the observational data

x (H)	2.00	2.20	2.40	2.80	3.20	3.60	2.00	2.16	2.32	2.48	2.64	2.80	3.00	3.20
z (H)	0.28	0.28	0.28	0.28	0.28	0.28	0.08	0.08	0.08	0.08	0.08	0.08	0.08	0.08
σ_{ys} (H)	0.3188	0.3293	0.3394	0.3587	0.3769	0.3943	0.3048	0.3138	0.3224	0.3308	0.3389	0.3466	0.3557	0.3642
σ_{ym} (H)	0.6375	0.7049	0.7536	0.7600	0.7698	0.8634	0.6342	0.6754	0.6628	0.7011	0.7083	0.7556	0.7486	0.6960
γ	0.2501	0.2182	0.2029	0.2228	0.2397	0.2085	0.2310	0.2159	0.2366	0.2226	0.2290	0.2104	0.2258	0.2738

In the present case, the average correction factor γ is 0.2277. This value is used to conduct another simulation of the isolated obstacle. The results are represented by dashed lines in Figs. 9 and 10. The simulation predicted the shape and spread much better. In the region close to the leeward side of the obstacle (Figs. 9a, 9b, 10a, and 10b), the simulation also showed good prediction of the peak values. However, it underestimated the concentration in other regions not close to the leeward side of the obstacle (Figs. 9c–f and Figs. 10c–f).

The underestimation may have several reasons: 1) the point source assumption, which does not exactly match the real condition because the recirculation region behind the obstacle is relatively broad; 2) the assumption of Gaussian-distributed concentration in spanwise (y) direction, which implies homogeneous turbulent diffusivity (μ_t and Γ_C) in the same direction, while Fig. 16 shows the heterogeneity of predicted turbulent diffusivity, which is obviously against the above assumption. It is also noted in Fig. 16 that the heterogeneity decreases as x/H increases, indicating that the choice of standard deviation of displacement in spanwise (y) direction from a much larger x may result in a better correction of turbulent Schmidt number. Unfortunately, no measured data were available at $x/H > 3.6$ in this dataset, which may need a future investigation; 3) use of a constant turbulent Schmidt number as used in most CFD approaches, but many investigations (e.g., Koeltzsch, 2000; Tominaga and Stathopoulos, 2007) indicated that turbulent Schmidt number is not a constant and depends on the local flow characteristics.

The corrected turbulent Schmidt number obtained above was also applied in another simulation for the case of an array of obstacles, since they shared the same experimental parameters. The simulation generally predicted much better results in terms of both the spread and the peak values, especially in the middle (Figs. 15c and 15d) of the source building and the building behind. However, we still need to take this result carefully because of the underestimation of the peak concentration in the isolated obstacle simulation with corrected turbulent Schmidt number.

5. Conclusions

A framework, based on a CFD approach solving steady-state RANS equations with the standard k-ε turbulence model, has been developed to simulate the flow, turbulence, and dispersion fields in urban builtup areas. Transport and dispersion modeling is made by solving an unsteady Eulerian transport equation using the velocity and turbulence field obtained from the steady RANS solution. The validation compares simulated to measured velocity, turbulence, and dispersion fields for the neutral flow in a series wind tunnel experiments conducted by Environmental Wind Tunnel Laboratory in University Hamburg.

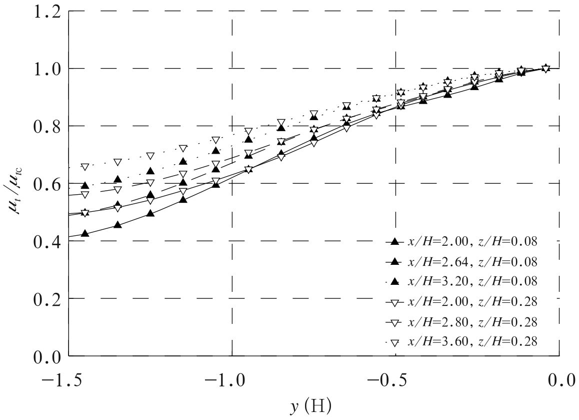

Fig. 16. Normalized turbulent diffusivity of momentum in spanwise (y) direction in the case of an isolated obstacle. Note: μ_{tc} is the turbulent diffusivity at $y/H = 0$.

It is found that the approach is able to predict the velocity fields very well both above and below the building height for the majority of simulated results.

The simulated TKE also corresponds to the measured one in both the shape and the location of the peak, although the TKE values are not predicted as good as those of wind velocity.

Without the correction of turbulent Schmidt number, the spread of simulated concentration fields is underestimated by the model. All peak values in spanwise (y) direction are overestimated in the simulation with an isolated obstacle, while in the case of an array of obstacles, the peak values near the leeward side of the source obstacle are overestimated, but those in the middle of the source obstacle and the obstacle behind are underestimated. Both cases with the correction of turbulent Schmidt number show a better spread prediction, especially the array of obstacles case, while the prediction of the isolated obstacle case underestimates the value of tracer concentration in the areas far ($x/H > 1$) from the source obstacle. The imperfect point sources, heterogeneous turbulent diffusivity, and the constant turbulent Schmidt assumption used in the simulations may be responsible for the underestimation of the concentration spread.

Future work will focus on applying this CFD approach in real urban regions, as well as the application of more sophisticated turbulent closure, and a more comprehensive treatment of the turbulent Schmidt number problem.

Acknowledgments. We would like to acknowledge the Environmental Wind Tunnel Laboratory in University Hamburg for offering measured data on the Internet.

REFERENCES

Cheng, Y., F. S. Lien, E. Yee, et al., 2003: A comparison of large Eddy simulations with a standard k-ε Reynolds-averaged Navier-Stokes model for the prediction of a fully developed turbulent flow over a matrix of cubes. *Journal of Wind Engineering and Industrial Aerodynamics*, **91**, 1301–1328.

Coirier, W. J., D. M. Fricker, M. Furmanczyk, et al., 2005: A computational fluid dynamics approach for urban area transport and dispersion modeling. *Environmental Fluid Mechanics*, **5**(5), 443–479.

Davidson, M. J., W. H. Snyder, R. E. Lawson, et al., 1996: Wind tunnel simulations of plume dispersion through groups of obstacles. *Atmos. Environ.*, **30**(22), 3715–3731.

Di Sabatino, S., R. Buccolieri, B. Pulvirenti, et al., 2007: Simulations of pollutant dispersion within idealised urban-type geometries with CFD and integral models. *Atmos. Environ.*, **41**(37), 8316–8329.

Flesch, T. K., J. H. Prueger, and J. L. Hatfield, 2002: Turbulent Schmidt number from a tracer experiment. *Agricultural and Forest Meteorology*, **111**(4), 299–307.

Gousseau, P., B. Blocken, T. Stathopoulos, et al., 2011: CFD simulation of near-field pollutant dispersion on a high-resolution grid: A case study by LES and RANS for a building group in downtown Montreal. *Atmos. Environ.*, **45**(2), 428–438.

Gromke, C., R. Buccolieri, S. Di Sabatino, et al., 2008: Dispersion study in a street canyon with tree planting by means of wind tunnel and numerical investigations–Evaluation of CFD data with experimental data. *Atmos. Environ.*, **42**(37), 8640–8650.

Hanna, S. R., M. J. Brown, F. E. Camelli, et al., 2006: Detailed simulations of atmospheric flow and dispersion in downtown Manhattan: An application of five computational fluid dynamics models. *Bull. Amer. Meteor. Soc.*, **87**(12), 1713–1726.

Higson, H. L., R. F. Griffiths, C. D. Jones, et al., 1995: Effect of atmospheric stability on concentration fluctuations and wake retention times for dispersion in the vicinity of an isolated building. *Environmetrics*, **6**(6), 571–581.

Koeltzsch, K., 2000: The height dependence of the turbulent Schmidt number within the boundary layer. *Atmos. Environ.*, **34**(7), 1147–1151.

Krüs, H. W., J. O. Haanstra, R. van der Ham, et al., 2003: Numerical simulations of wind measurements at Amsterdam Airport Schiphol. *Journal of Wind Engineering and Industrial Aerodynamics*, **91**(10), 1215–1223.

Launder, B. E., and D. B. Spalding, 1974: The numerical computation of turbulent flows. *Computer Methods in Applied Mechanics and Engineering*, **3**(2), 269–289.

Li, X. X., C. H. Liu, D. Y. C. Leung, et al., 2006: Recent progress in CFD modeling of wind field and pollutant transport in street canyons. *Atmos. Environ.*, **40**(29), 5640–5658.

Macdonald, R. W., R. F. Griffiths, and S. C. Cheah, 1997: Field experiments of dispersion through regular arrays of cubic structures. *Atmos. Environ.*, **31**(6), 783–795.

——, ——, and D. J. Hall, 1998: A comparison of results from scaled field and wind tunnel modeling of dispersion in arrays of obstacles. *Atmos. Environ.*, **32**(22), 3845–3862.

Mavroidis, I., 2000: Velocity and concentration measurements within arrays of obstacles. *Global Nest: the Int. J.*, **2**(1), 109–117.

——, R. F. Griffiths, and D. J. Hall, 2003: Field and wind tunnel investigations of plume dispersion around single surface obstacles. *Atmos. Environ.*, **37**(21), 2903–2918.

——, S. Andronopoulos, J. G. Bartzis, et al., 2007: Atmospheric dispersion in the presence of a three-dimensional cubical obstacle: Modeling of mean concentration and concentration fluctuations. *Atmos. Environ.*, **41**(13), 2740–2756.

Nozawa, K., and T. Tamura, 2002: Large eddy simulation of the flow around a low-rise building immersed in a rough-wall turbulent boundary layer. *Journal of Wind Engineering and Industrial Aerodynamics*, **90**(10), 1151–1162.

Riddle, A., D. Carruthers, A. Sharpe, et al., 2004: Comparisons between FLUENT and ADMS for atmospheric dispersion modeling. *Atmos. Environ.*, **38**(7), 1029–1038.

Santos, J. M., N. C. Reis, E. V. Goulart, et al., 2009: Numerical simulation of flow and dispersion around an isolated cubical building: The effect of the atmospheric stratification. *Atmos. Environ.*, **43**(34), 5484–5492.

Solazzo, E., S. Vardoulakis, and X. M. Cai, 2011: A novel methodology for interpreting air quality measurements from urban streets using CFD modeling. *Atmos. Environ.*, **45**(29), 5230–5239.

Stull, R. B., 1988: *An Introduction to Boundary Layer Meteorology.* Kluwer Academic Publishers, 181 pp.

Sykes, R. I., and R. S. Gabruk, 1997: A second-order closure model for the effect of averaging time on turbulent plume dispersion. *J. Appl. Meteor.*, **36**(8), 1038–1045.

Tewari, M., H. Kusaka, F. Chen, et al., 2010: Impact of coupling a microscale computational fluid dynamics model with a mesoscale model on urban scale contaminant transport and dispersion. *Atmos. Res.*, **96**(4), 656–664.

Tominaga, Y., and T. Stathopoulos, 2007: Turbulent Schmidt numbers for CFD analysis with various types of flowfield. *Atmos. Environ.*, **41**(37), 8091–8099.

Versteeg, H. K., and W. Malalasekera, 2010: *An Introduction to Computational Fluid Dynamics: The Finite Volume Method.* World Publishing Corporation, 151–280.

Wang Fujun, 2004: *The Analysis of Computational Fluid Dynamics–The Theory and Application of CFD Software.* Tsinghua Press, Beijing, 36–83. (in Chinese)